

# A Novel High-Order Range Model and Imaging Approach for High-Resolution LEO SAR

Yunhua Luo, Bingji Zhao, Xiaolei Han, Robert Wang, *Senior Member, IEEE*,  
Hongjun Song, and Yunkai Deng, *Member, IEEE*

**Abstract**—High-resolution spaceborne synthetic aperture radar (SAR) mainly poses two challenges to signal processing. The first challenge involves the signal model, where a precise range equation of spaceborne SAR should be considered as the conventional hyperbolic range equation fails to precisely describe the range history in the high-resolution case. The second challenge is an efficient focusing algorithm since the existing SAR processors are inaccurate or inefficient for high-resolution spaceborne SAR. Therefore, in this paper, a novel fourth-order polynomial range equation based on Doppler parameters is proposed, and the method for parameter determination is also addressed. Compared with conventional range equations, the presented one is more accurate and concise for low-earth-orbit SAR so that a higher azimuth resolution can be achieved. Based on the range model, a 2-D spectrum is derived, and an extended range Doppler domain algorithm for SAR image formation in the sliding spotlight mode is also developed. Additionally, we carried out several simulations to validate the presented approach. Results demonstrate high performances of the focusing algorithm as well as the range equation.

**Index Terms**—Fourth-order Doppler range model (DRM4), high resolution, low earth orbit (LEO), range Doppler algorithm (RDA).

## I. INTRODUCTION

SINCE the first spaceborne synthetic aperture radar (SAR) (Seasat) was launched in 1978 [1], the developments of spaceborne SAR have achieved a great progress during the past decades. Several advanced spaceborne SAR systems, such as TerraSAR, COSMO-SkyMed, and RADARSAT2, have been in the orbit, providing plenty of information for ice forecasting, monitoring of coastal regions, assisting in disaster management, and protecting national sovereignty [2]–[7]. These SAR systems are different in terms of size, weight, and performances. However, all of them share the same type of orbit, namely, low earth orbit (LEO).

LEO is always preferred for spaceborne SAR orbit design considering the power supply and signal processing. On the one hand, the along-track variations of LEO are slighter with respect to that of medium earth orbit (MEO) and geosynchronous

earth orbit (GEO) [8], [9]. As a result, the conventional hyperbolic range equation (HRE) model can well represent SAR motion during the synthetic aperture time with the present resolution [10]–[12]. On the other hand, most of the classic SAR processors, such as the range Doppler algorithm (RDA), the chirp scaling algorithm, the wavenumber domain algorithm, and the variations, are all based on the imaging geometry of airborne SAR, where the trajectory of SAR is approximated to be a straight line during the integration time. Consequently, these algorithms can well accommodate the spaceborne SAR image formation with little modifications.

However, the future LEO SAR systems are characterized by high resolution, wide swath, and smart modes, where a long integration time is necessary to achieve high resolution. The long synthetic aperture time induces numerous problems for spaceborne SAR system design as well as signal processing. In this paper, we concentrate on the latter and therefore overcome two challenges. The first one is that the conventional HRE cannot precisely represent range history of high-resolution spaceborne SAR, and the second relates to an efficient focusing algorithm for LEO SAR.

For the first issue, the conventional HRE model that is widely used to process the existing spaceborne SAR data is derived from the straight track and is adapted to the curved orbit of spaceborne SAR by equivalent velocity and squint angle [10]–[12]. However, only Doppler centroid frequency and azimuth FM rate are employed in the equation, resulting in a large phase error in the high-resolution case. Consequently, the authors in [8] advocated an advanced HRE (AHRE) to describe the range history of MEO SAR. An additional linear term (with quadratic azimuth FM rate) is introduced into the conventional HRE so that it can handle the focusing issue of an azimuth resolution around 3 m at altitudes from 1000 to 10 000 km, whereas the situation of high-resolution LEO SAR was not discussed yet, and we demonstrate that the AHRE model fails in ultrahigh-resolution case in the study. Similarly, a fourth-order polynomial range equation for spaceborne SAR imaging, considering the rotation of the Earth, was proposed by Eldhuset, and a 2-D exact transfer function (ETF) was derived [13]. Nevertheless, the ETF was complex due to a sophisticated expression for the point of stationary phase which was solved by the conventional solution method for polynomial. Furthermore, only the case of resolution around 1 m was referred. Therefore, based on the previous work, a novel fourth-order Doppler range model (DRM4) is put forward to accurately represent the range equation of high-resolution LEO SAR, which can easily accommodate the signal description with the azimuth

Manuscript received January 11, 2013; revised April 26, 2013 and June 19, 2013; accepted June 26, 2013. Date of publication August 6, 2013; date of current version March 3, 2014. This work was supported in part by the “Hundred Talents Program” of the Chinese Academy of Sciences.

The authors are with the Department of Space Microwave Remote Sensing Systems, Institute of Electronics, Chinese Academy of Sciences, Beijing 100190, China (e-mail: csuluoyunhua@163.com; zachary\_zbj@163.com; hanxiaolei23@163.com; yuwang@mail.ie.ac.cn; hjsong@mail.ie.ac.cn; ykdeng@mail.ie.ac.cn).

Color versions of one or more of the figures in this paper are available online at <http://ieeexplore.ieee.org>.

Digital Object Identifier 10.1109/TGRS.2013.2273086

resolution below 0.3 m. Determining the Doppler parameters of the equation is the key issue of the proposed model, and we will analyze it in great detail in Section II.

Concerning the focusing algorithm for high-resolution spaceborne SAR, a few methods are proposed. Most of the existing algorithms are based on the conventional HRE, where the azimuth modulation phase and the range cell migration (RCM) are both presented by hyperbolic equalities. Thus, some methods can be utilized to improve the efficiency of the algorithms, such as chirp scaling, frequency scaling, chirp-z transformation, and Stolt interpolation. For example, the modified nonlinear chirp scaling is engaged to compensate the spatial variant cross-coupling phase between range and azimuth for spaceborne SAR signal processing [8]. The polar format algorithm was also refined by Chen to suit for data processing in spaceborne SAR [14]. However, an accurate range equation of high-resolution spaceborne SAR is beyond the considerations of these algorithms. The back projection algorithm can precisely focus the raw data of high-resolution LEO SAR, while the computation load is too huge to fulfill [15]–[17]. In our proposed range equation, the Doppler parameters are both spatial variant in the range and azimuth directions, leading to different characteristics of azimuth phase history and RCM from the conventional HRE. As a result, the existing imaging algorithms for spaceborne SAR signal processing cannot be directly applied to the presented case, and a new efficient method is urgently desired. In the presented work, we derive the point target reference spectrum (PTRS) of signal with DRM4, where a concise expression is obtained by the method of series reversion (MSR). Based on the analysis of the Doppler parameters in DRM4, an extended range Doppler domain algorithm is proposed to efficiently focus the raw data, and the simulation experiments validate the focusing approach.

This paper proceeds as follows. In Section II, we investigate the accurate signal model of LEO SAR, where the conventional HRE is briefly introduced and the proposed DRM4 is presented, as well as the PTRS model. The corresponding imaging algorithm in high-resolution sliding spotlight mode is developed in Section III. Simulation experiments with a large extent scene are performed in Section IV to validate the presented method. Finally, the conclusion and a future work are summarized in Section V.

## II. SIGNAL MODEL

### A. Conventional HRE

The conventional HRE, widely used for the existing LEO SAR signal processing, takes the actual path of the satellite as a straight line in the imaging geometry, while the curved orbit of the satellite is compensated by equivalent velocity and squint angle. The range equation can be expressed as

$$R(\eta) = \sqrt{r_c^2 + v_r^2 \eta^2 - 2r_c v_r \sin \theta_{sq} \eta} \quad (1)$$

where  $r_c$  denotes the center range at Doppler center time and  $\eta$  is the azimuth time.  $v_r$  is the equivalent radar velocity, while  $\theta_{sq}$  represents the equivalent squint angle induced by the motion of the satellite and the rotation of the Earth.

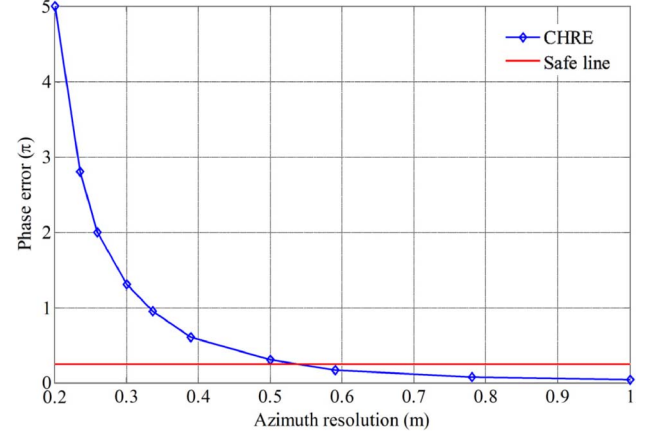


Fig. 1. Phase error induced by the range deviation as a function of azimuth resolution in conventional HRE.

In the procedure of imaging processing, the equivalent velocity and squint angle are calculated by [18]–[20]

$$\begin{cases} v_r = \sqrt{\left(\frac{\lambda f_{dc}}{2}\right)^2 - \frac{\lambda r_c f_{1r}}{2}} \\ \theta_{sq} = \arcsin\left(\frac{\lambda f_{dc}}{2v_r}\right) \end{cases} \quad (2)$$

where  $f_{dc}$  represents the Doppler centroid frequency and  $f_{1r}$  denotes the azimuth FM rate. These Doppler parameters can be estimated from raw data or the satellite attitude and beam pointing measurements.

Equation (2) shows that only the Doppler centroid and the azimuth FM rate are engaged in the conventional HRE, which is not sufficient for the range history description of high-resolution spaceborne SAR. A simulation is performed with orbit parameters described in Section IV to evaluate the performance of the HRE model. The maximal phase error in the whole orbit period induced by the range deviation as a function of azimuth resolution is sketched in Fig. 1, where the slant range calculated by numerical method is referred.

From Fig. 1, it can be observed that the maximal phase error caused by the conventional HRE model is greater than  $\pi/4$ , with the worst azimuth resolution (in the whole orbit duty) of 0.5 m. Nevertheless, the resolution cannot meet the requirement of the future applications yet since a higher resolution has been reached [21]. Thereby, the conventional HRE would be in dilemma in the case of high resolution, and a more accurate range model is urgently desired.

### B. DRM4

Compared with the conventional HRE, the proposed DRM4 utilizes fourth-order Doppler parameters to accurately describe the range history of high-resolution LEO SAR, ensuring much higher azimuth resolution. The proposed range equation model is presented using four parameters  $k_1, k_2, k_3, k_4$ , i.e.,

$$R(\eta) = r_0 + k_1 \eta + k_2 \eta^2 + k_3 \eta^3 + k_4 \eta^4 \quad (3)$$

where  $r_0$  is the slant range of the closest approach and  $k_1, k_2, k_3, k_4$  are the first-order, second-order, third-order, and fourth-order Doppler parameters, respectively. Determining the

parameters is the key issue of the proposed range model since all of the parameters are both varying in the azimuth and range directions in high-resolution spaceborne SAR. In fact, an analytical method has been presented in solving the issue.

In [22], the author proposed an accurate fourth-order Doppler parameter calculation approach for GEO SAR based on the state vectors of the satellite and targets, including the range vector, velocity vector, and acceleration vector, where the two-body model and the rotation of the Earth are considered. The attitude of the satellite is actively controlled by attitude steering so that the Doppler offset is reduced to be nearly zero [23]. By calculating the instantaneous range vectors and velocity vectors as well as the acceleration vectors between the satellite and ground targets in Earth-centered inertial coordinate system, the Doppler parameters in DRM4 can be obtained by the following equations:

$$f_{dc} = -\frac{2\mathbf{R}'}{\lambda} = -\frac{2(\mathbf{r}_s - \mathbf{r}_t)(\mathbf{v}_s - \mathbf{v}_t)}{\lambda R} \quad (4)$$

$$f_{1r} = -\frac{2\mathbf{R}''}{\lambda} = -\frac{2}{\lambda} \left[ \frac{(\mathbf{v}_s - \mathbf{v}_t)^2}{R} + \frac{(\mathbf{A}_s - \mathbf{A}_t)(\mathbf{r}_s - \mathbf{r}_t)}{R} - \frac{\lambda^2 f_{dc}^2}{4R} \right] \quad (5)$$

$$f_{2r} = -\frac{2\mathbf{R}^{(3)}}{\lambda} = -\frac{2}{\lambda} \left[ \frac{3(\mathbf{v}_s - \mathbf{v}_t)(\mathbf{A}_s - \mathbf{A}_t)}{R} + \frac{(\mathbf{r}_s - \mathbf{r}_t)(\mathbf{A}'_s - \mathbf{A}'_t)}{R} - \frac{3\lambda^2 f_{dc} f_{1r}}{4R} \right] \quad (6)$$

$$f_{3r} = -\frac{2\mathbf{R}^{(4)}}{\lambda} = -\frac{2}{\lambda} \left[ \frac{3(\mathbf{A}_s - \mathbf{A}_t)^2}{R} + \frac{4(\mathbf{v}_s - \mathbf{v}_t)(\mathbf{A}'_s - \mathbf{A}'_t)}{R} + \frac{(\mathbf{r}_s - \mathbf{r}_t)(\mathbf{A}''_s - \mathbf{A}''_t)}{R} - \frac{3\lambda^2 f_{1r}^2}{4R} - \frac{\lambda^2 f_{dc} f_{2r}}{R} \right] \quad (7)$$

where  $R$  is the range between the satellite and ground target.  $\mathbf{r}$ ,  $\mathbf{v}$ ,  $\mathbf{A}$ ,  $\mathbf{A}'$ , and  $\mathbf{A}''$  are all state vectors and represent the 3-D position vector, velocity vector, acceleration vector, rate of the acceleration vector, and rate of the rate of the acceleration vector, respectively. The subscript  $s$  means the satellite, and  $t$  represents ground target.  $f_{2r}$  denotes the rate of the FM rate, and  $f_{3r}$  stands for the rate of the rate of the FM rate. Consequently, the parameters  $k_1, k_2, k_3, k_4$  can be expressed as  $k_1 = -\lambda f_{dc}/2$ ,  $k_2 = -\lambda f_{1r}/4$ ,  $k_3 = -\lambda f_{2r}/12$ , and  $k_4 = -\lambda f_{3r}/48$ , respectively. Since there is no difference between LEO SAR and GEO SAR in the derivation of the Doppler parameters, they can be directly applied in calculating the parameters of DRM4 in high-resolution LEO SAR signal processing.

With the Doppler parameters listed in (4)–(7), a simulation is followed to evaluate the accuracy of DRM4, AHRE, and HRE, where the phase error due to range deviations is used as criterion. The simulation parameters are listed in Section IV, and the result obtained by numerical method is taken as reference.

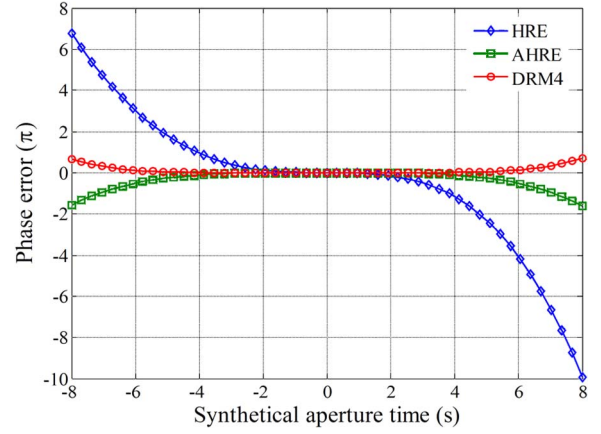


Fig. 2. Phase error induced by the slant range error as a function of synthetical aperture time in DRM4/AHRE/HRE.

From Fig. 2, it can be seen that the proposed DRM4 enjoys the highest performance compared with the HRE and AHRE models. The conventional HRE model can accommodate about 4.8-s integration time, while the maximal synthetic aperture time for the AHRE model is less than 9.9 s, corresponding to azimuth resolution around 0.17 m. However, with the proposed DRM4 model, the integration time is up to 13.4 s. As a result, an azimuth resolution that is better than 0.13 m can be achieved by DRM4, which can meet the requirements of most future applications in spaceborne SAR.

Therefore, with the method presented in this section, the Doppler parameters can be solved, and thus, a more accurate and efficient range equation for high-resolution LEO SAR is fulfilled.

### C. Analysis for DRM4

DRM4 is illustrated in the previous section, and the method for parameter determination is also prepared. In this section, we analyze the characteristics of the proposed DRM4 in LEO SAR, where the Doppler parameters are emphasized. The variations of the fourth-order Doppler parameters in the azimuth time are given in Fig. 3. The simulation parameters of orbit are described in Section IV, and the swath width is about 10 km.

In the proposed DRM4, the Doppler offset is compensated by attitude steering, leading to tiny Doppler centroid in Fig. 3(a). In fact, a very small Doppler offset usually remains in practice due to the accuracy of antenna steering as Fig. 4(a) shows, where the Doppler offset of TSX-1 in strip-map mode is depicted. The Doppler rate, which is the most important for DRM4, is also plotted in Fig. 3(b), demonstrating only 0.007% deviation from the average value during the azimuth time. As a result, we may assume that it is invariant during the integration time to facilitate the corresponding imaging algorithm design. Details on the assumption are discussed in Appendix A. The Doppler rate variations of TSX-1 in Fig. 4(b) validate the little deviation of Doppler rate. Similarly, we can observe that the second- and third-order Doppler parameters of DRM4 also slightly vary with the azimuth time. Thereby, it is possible to explore an efficient focusing algorithm for DRM4 without segmenting in the azimuth direction under this assumption. We discuss the issue in Section III.



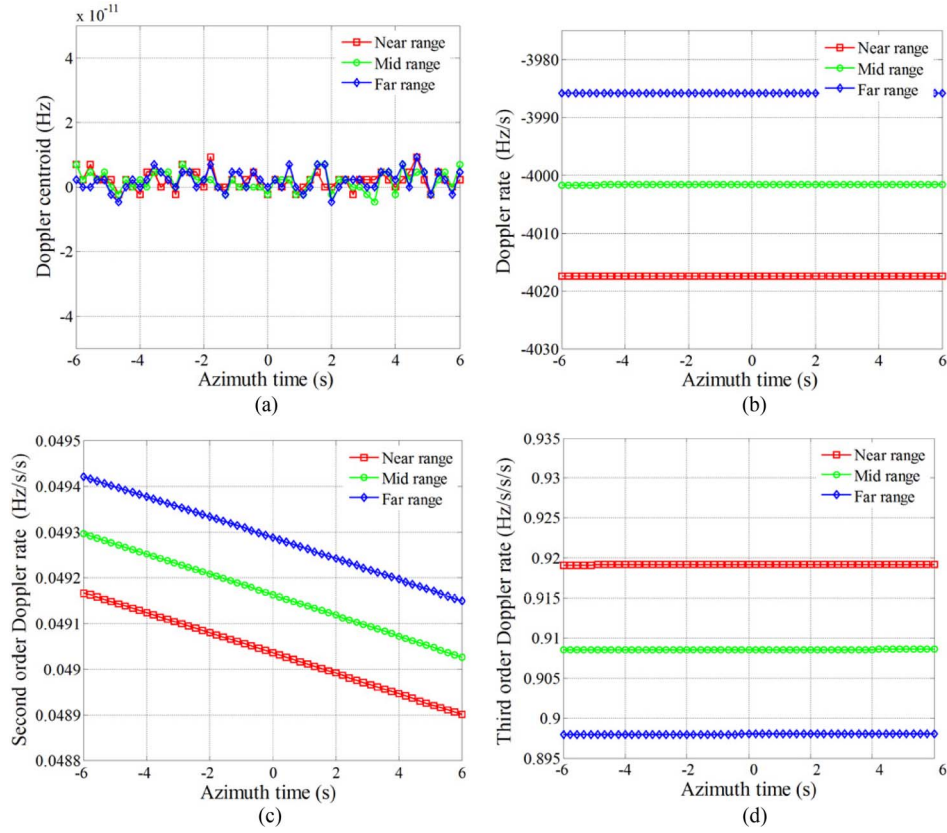


Fig. 3. (a) Doppler centroid variation. (b) Doppler rate variation. (c) Second-order Doppler rate variation. (d) Third-order Doppler rate variation.

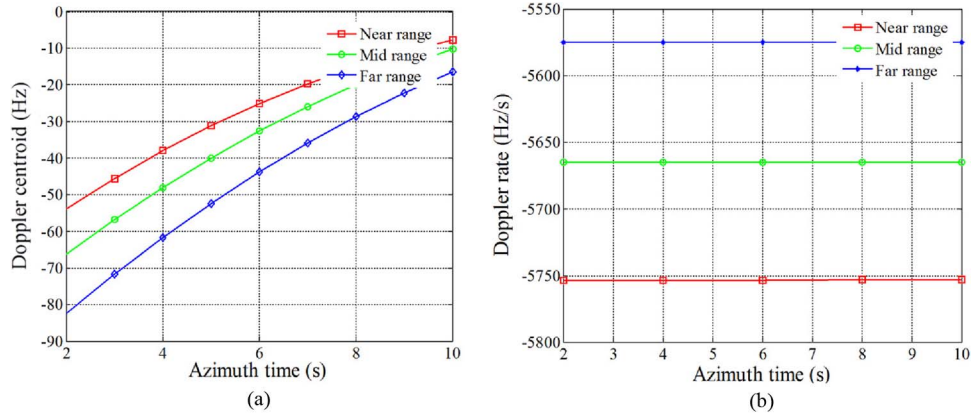


Fig. 4. (a) Doppler centroid of TSX-1. (b) Doppler rate of TSX-1.

#### D. PTRS for DRM4

We concentrate on the accurate signal model of high-resolution LEO SAR in this section. With the range (3), we can write the received echo of spaceborne SAR as

$$S(t, \eta) = \sigma_0 w_r \left( t - \frac{2R(\eta)}{c} \right) \cdot w_a(\eta - \eta_0) \cdot \exp \left\{ -j \frac{4\pi f_c R(\eta)}{c} \right\} \cdot \exp \left\{ j\pi K_r \left[ t - \frac{2R(\eta)}{c} \right]^2 \right\} \quad (8)$$

where  $\sigma_0$  represents the scattering coefficient and  $w_r(\cdot)$ ,  $w_a(\cdot)$  are antenna pattern functions in the range and azimuth directions, respectively.  $f_c$  stands for the carrier frequency, and  $c$  is

the speed of light.  $K_r$  is the range chirp rate.  $t$  is the fast time, and  $\eta_0$  denotes the Doppler center time of point target.

After the introduction of the signal model, the PTRS is investigated. We perform range Fourier transformation (FT) on (8) and utilize the principle of stationary phase to solve it. Then, the signal in the range frequency domain can be obtained as

$$S(f_r, \eta) = \sigma_0 w_r(f_r) \cdot w_a(\eta - \eta_c) \cdot \exp \left\{ -j \frac{\pi f_r^2}{K_r} \right\} \cdot \exp \left\{ -j \frac{\pi (f_c + f_r) R(\eta)}{c} \right\}. \quad (9)$$

The 2-D spectrum can be acquired by azimuth FT on (9), whereas the existence of the high-order term of  $\eta$  in  $R(\eta)$  makes

it complex to directly solve the point of stationary phase [13]. As an alternative, MSR is introduced [25]. By using MSR to solve the point of stationary phase in the azimuth direction, a concise 2-D spectrum can be yielded

$$S(r_0, f_r, f_\eta) = \sigma_0 w_r(f_r) \cdot w_a(f_\eta - f_{dc}) \cdot \exp \{f \Phi_{PTRS}(r_0, f_r, f_\eta)\} \quad (10)$$

$$\Phi_{PTRS}(r_0, f_r, f_\eta) \approx -\frac{4\pi(f_c + f_r)}{c}(r_0 - M^2\alpha_0/2 - M^3\beta_0/3 - M^4\gamma_0/4) - \pi f_r^2/K_r \quad (11)$$

where  $M = -cf_\eta/(2(f_c + f_r)) + \lambda f_{dc}/2$  and  $f_\eta \in (-PRF/2, PRF/2)$ .  $\alpha_0, \beta_0, \gamma_0$  are the Doppler parameters of the range equation of point target at the nearest range  $r_0$ , all of which are spatial variant in range and azimuth. They can be calculated as  $\alpha_0 = 1/2k_2$ ,  $\beta_0 = -k_3/8k_2^3$ , and  $\gamma_0 = (9k_3^2 - 4k_2k_4)/16k_2^5$ .

#### E. Expanded PTRS for DRM4

The PTRS model of DRM4 is presented in (10) and (11), where the cross-coupling between range and azimuth is described by a fourth-order polynomial, whereas it is not a proper form for analyzing the characteristics of the spectrum as well as developing an efficient imaging algorithm in frequency algorithm. As a consequence, the PTRS model is expanded by power series with respect to  $f_r$  [26]. We label the zero-order term as  $\Phi_{azi}$ , which presents azimuth modulation. The first-order phase is denoted as  $\Phi_{RCM}$ , describing RCM. We name the second-order phase as  $\Phi_{az\_rg2}$ , which contains the range modulation phase and second-order cross-coupling, while the third-order one is labeled as  $\Phi_{az\_rg3}$ , which describes the third-order coupling phase. These terms are defined in

$$\Phi_{azi}(r_0, f_r, f_\eta) = \frac{4\pi}{\lambda} \left[ -r_0 + \frac{\lambda^2(f_\eta - f_{dc})^2}{8}\alpha_0 - \frac{\lambda^3(f_\eta - f_{dc})^3}{24}\beta_0 + \frac{\lambda^4(f_\eta - f_{dc})^4}{64}\gamma_0 \right] \quad (12)$$

$$\Phi_{RCM}(r_0, f_r, f_\eta) = -\frac{4\pi}{c} \left\{ r_0 + \frac{\lambda^2[(f_\eta - f_{dc})^2 + 2f_{dc}(f_\eta - f_{dc})]}{8}\alpha_0 - \frac{\lambda^3[2(f_\eta - f_{dc})^3 + 3f_{dc}(f_\eta - f_{dc})^2]}{24}\beta_0 + \frac{\lambda^4[3(f_\eta - f_{dc})^4 + 4(f_\eta - f_{dc})^3]}{64}\gamma_0 \right\} \cdot f_r \quad (13)$$

$$\Phi_{az\_rg2}(r_0, f_r, f_\eta) = -\frac{\pi f_r^2}{K_r} + \pi \left[ \frac{\lambda f_\eta^2}{2f_c^2}\alpha_0 - \frac{\lambda^2 f_\eta^2(f_\eta - f_{dc})}{2f_c^2}\beta_0 + \frac{3\lambda^3 f_\eta^2(f_\eta - f_{dc})^2}{8f_c^2}\gamma_0 \right] \cdot f_r^2 \quad (14)$$

$$\Phi_{az\_rg3}(r_0, f_r, f_\eta) = -\pi \left\{ \frac{\lambda f_\eta^2}{2f_c^3}\alpha_0 - \frac{\lambda^2 f_\eta^2[4(f_\eta - f_{dc}) + f_{dc}]}{6f_c^3}\beta_0 + \frac{\lambda^3 f_\eta^2[5(f_\eta - f_{dc})^2 + 2f_{dc}(f_\eta - f_{dc})]}{8f_c^3}\gamma_0 \right\} \cdot f_r^3 \quad (15)$$

respectively.

Some remarks would facilitate a better understanding of the characteristics of the expanded spectrum.

- 1) The azimuth phase in (12) is accurately described by a fourth-order polynomial, which is hyperbolic in HRE. In addition, the phase varies with  $\alpha_0, \beta_0, \gamma_0$  in 2-D space domain, leading to the azimuth matched filter tough in the range Doppler domain. An approach to the solution of this problem is presented in the next section under an assumption.
- 2) Expression (13) represents the RCM phase. Compared with RCM in HRE, the RCM in DRM4 is also represented by spatial variant parameters  $\alpha_0, \beta_0, \gamma_0$  so that it is hard to precisely correct it by an efficient way such as chirp scaling and chirp-z. Instead, interpolation is employed to cope with this issue.
- 3) The second-order and third-order cross-couplings are presented in (14) and (15). While they are useful to illustrate the spectrum characteristics of DRM4, it would not be utilized to compensate the high-order coupling in the case of high-resolution spaceborne SAR owing to its poor accuracy. We analyze the effects of these terms in Appendix B.

By expanding the PTRS model in DRM4 with power series, the phase terms in conventional focusing algorithms are obtained, and it proves to be very helpful in developing a new efficient and precise focusing algorithm. We illustrate it in the following section.

### III. IMAGING APPROACH

The signal model has been discussed, and a new slant range equation for high-resolution spaceborne SAR is put forward in Section II. Based on the proposed model, we concentrate on the corresponding imaging algorithm in this section. As a large azimuth bandwidth is required for high resolution, the sliding spotlight mode is advised for spaceborne SAR to alleviate the need for high PRF. We first introduce the imaging geometry of high-resolution spaceborne sliding spotlight SAR in Section III-A, where the differences from the conventional

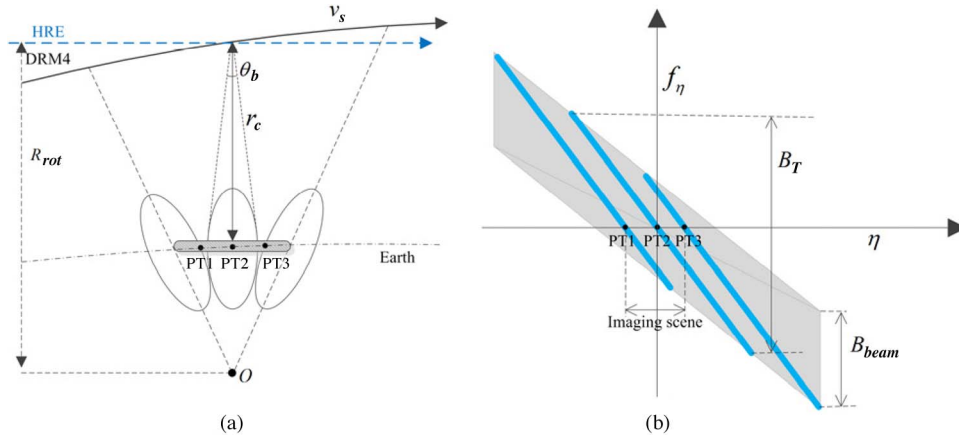


Fig. 5. (a) Imaging geometry of the sliding spotlight SAR. (b) Time frequency diagram of the sliding spotlight SAR.

sliding spotlight mode are emphasized. In Section III-B, an extended range Doppler domain algorithm is developed to focus the raw data.

#### A. Imaging Geometry

As described in Section II, in DRM4, the spatial variations of the Doppler parameters in the range and azimuth directions are both taken into account. Thus, compared to the HRE model for airborne and spaceborne SAR, the curved orbit is emphasized in Fig. 5(a), where  $v_s$  is the velocity of the satellite,  $\theta_b$  stands for the beam width,  $r_c$  is the middle range of the imaging scene, and  $R_{rot}$  is the rotation slant range with rotation center of  $O$ . Three point targets PT1, PT2, and PT3 are set in the imaging geometry to evaluate the azimuth extent of the proposed imaging approach.

In the data acquisition of the sliding spotlight SAR, the main beam of the antenna is steering to a fixed point, namely, the rotation center. As a consequence, the time frequency diagrams of the point targets vary with the azimuth locations as illustrated in Fig. 5(b), where  $B_T$  denotes the azimuth bandwidth of the point target that is much higher than PRF in spotlight and sliding spotlight modes and  $B_{beam}$  is the instantaneous bandwidth of the antenna beam. It can be observed from Fig. 5(b) that PT1, PT2, and PT3 enjoy different Doppler centroids owing to different squint angles for each target. As a result, it requires that the proposed PTRS and the focusing method can accommodate the case of low squint. We validate it in Appendix B.

#### B. Imaging Algorithm

In this section, an extended range Doppler domain algorithm is presented to focus the raw data of the high-resolution sliding spotlight spaceborne SAR. Before introducing the algorithm, note that the Doppler parameters of the proposed range equation in LEO SAR slightly vary in the azimuth direction but much lie on the range locations as shown in Fig. 3, which means that it is possible to ignore the azimuth spatial variations of the parameters of DRM4 for all targets in the imaging algorithm. Then, we can design an efficient focusing algorithm without segmenting in the azimuth direction. The assumption

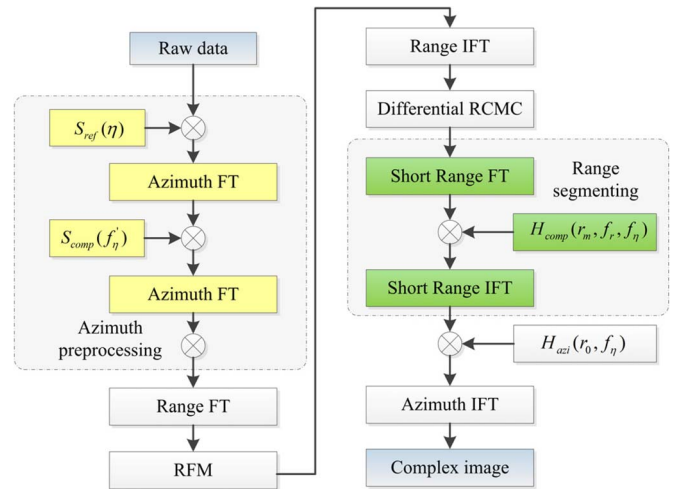


Fig. 6. Block diagram of the extended range Doppler domain algorithm.

is verified in Appendix A. Consequently, an extended range Doppler domain algorithm is put forward in Fig. 6.

The proposed algorithm includes three parts. The first part, based on the conventional two-step method [27], is used to remove azimuth aliasing in the sliding spotlight mode. The second one is the extended range Doppler domain algorithm that can accommodate the RCM and azimuth modulation in DRM4. The last part provides the capability of wide-swath imaging for the presented algorithm, where the cross-coupling phase is compensated by segmenting in the range direction. We illustrate these parts in the following.

1) *Azimuth Preprocessing*: During the data acquisition of the sliding spotlight SAR, the steering of the antenna main beam introduces extra bandwidth that may be several times of the instantaneous bandwidth of the beam. As a result, severe azimuth aliasing occurs, especially in the case of high resolution. To remove the aliasing, two methods are usually adopted. One is the subaperture method [28], where the raw data are divided into small segments in the azimuth time domain, and then, we perform focusing and residual correction on each segment. However, meticulous bookkeeping of indexes is required when the segments are added coherently. The other way is the two-step processing approach to accommodate the bandwidth of the point target by scaling.

In the mentioned situation, a very long synthetic aperture is employed, and a large Doppler centroid difference is produced between subapertures as shown in Fig. 5(b), which would make the subaperture method tough and complex. Therefore, the latter method is preferred in the proposed algorithm for the azimuth preprocessing. The two-step approach is illustrated in [27]; however, for the case of high resolution and large azimuth extent, two points should be emphasized.

The conventional reference function  $S_{\text{ref}}(\eta)$  in the azimuth preprocessing would introduce a residual azimuth bandwidth after convolution, which varies with range frequency and can be expressed as follows [29]

$$B_{\text{res}} = \frac{2v_s}{L} + \left[ \frac{(1-a)v_s^2 T_{\text{sar}}}{cr_0} + \frac{\theta_b v_s}{c} \right] B_r \quad (16)$$

where  $L$  is the antenna length,  $a$  denotes the sliding factor,  $T_{\text{sar}}$  is the synthetic aperture time, and  $B_r$  stands for the transmitted bandwidth. In the presence of large chirp bandwidth, the residual azimuth bandwidth would lead to azimuth aliasing again, and thus, a much higher PRF would be required. Fortunately, we can greatly alleviate the azimuth aliasing with a range-frequency-dependent reference function in azimuth preprocessing, resulting in a reduced computation load in signal processing [30]. The second point is that the Doppler centroid variations induced by the azimuth extent would lead to extra azimuth bandwidth and should be taken into account in the system parameter design.

2) *Extended Range Doppler Domain Algorithm*: The classic RDA is based on the conventional HRE, where hyperbolic RCM and azimuth modulation are involved. However, the characteristics of the signal of DRM are totally different from that in the conventional HRE. Therefore, the conventional focusing algorithm based on HRE cannot deal with the imaging issue in DRM4. In this section, an extended range Doppler domain algorithm is put forward to process the signal in DRM4. The steps of the algorithm are illustrated as follows.

The algorithm begins with reference function multiplication (RFM) in wavenumber domain. The RCM and azimuth modulation as well as high-order cross-coupling at the reference slant range are removed. The reference function is described as

$$H_{\text{RFM}}(r_{\text{ref}}, f_r, f_\eta) = \exp \left\{ j \frac{4\pi(f_c + f_r)}{c} \left( r_{\text{ref}} - \frac{M^2}{2} \alpha_{\text{ref}} - \frac{M^3}{3} \beta_{\text{ref}} - \frac{M^4}{4} \gamma_{\text{ref}} \right) \right\} \cdot \exp \left\{ j \frac{\pi f_r^2}{K_r} \right\} \quad (17)$$

where  $r_{\text{ref}}$  is the reference slant range, and it is usually chosen as the middle slant range of the scene. The corresponding parameters are  $\alpha_{\text{ref}}$ ,  $\beta_{\text{ref}}$ , and  $\gamma_{\text{ref}}$ . The residual phase of the signal after RFM can be expressed as

$$\Phi_{\text{RFM}}(r_0, f_r, f_\eta) = \frac{4\pi(f_c + f_r)}{c} \left[ (r_{\text{ref}} - r_0) + \frac{M^2}{2} (\alpha_0 - \alpha_{\text{ref}}) + \frac{M^3}{3} (\beta_0 - \beta_{\text{ref}}) + \frac{M^4}{4} (\gamma_0 - \gamma_{\text{ref}}) \right]. \quad (18)$$

After computing the range inverse FT (IFT) of the signal, the signal is range compressed, and we can correct the residual RCM in the range Doppler domain. As we discussed in the previous work, the RCM in DRM4 is spatial variant and so is the residual RCM. Although linear fitting of the RCM may help to improve the efficiency at the cost of accuracy, the general case of LEO SAR is considered in our approach; thus, sinc interpolation is utilized to correct the residual RCM. In order to get an accurate result, an interpolation kernel with more than eight points is advised for the high-resolution case. According to (12)–(15), the differential RCM in the range Doppler domain is formulated as

$$\begin{aligned} \text{RCM}_{\text{diff}}(r_0, f_\eta) &= -\frac{\lambda^2 [(f_\eta - f_{\text{dc}})^2 + 2f_{\text{dc}}(f_\eta - f_{\text{dc}})]}{8} (\alpha_0 - \alpha_{\text{ref}}) \\ &\quad + \frac{\lambda^3 [2(f_\eta - f_{\text{dc}})^3 + 3f_{\text{dc}}(f_\eta - f_{\text{dc}})^2]}{24} (\beta_0 - \beta_{\text{ref}}) \\ &\quad - \frac{\lambda^4 [3(f_\eta - f_{\text{dc}})^4 + 4f_{\text{dc}}(f_\eta - f_{\text{dc}})^3]}{64} (\gamma_0 - \gamma_{\text{ref}}). \end{aligned} \quad (19)$$

After differential RCMC, all targets have their range migration trajectories equalized, and then, we can efficiently perform azimuth compression. Similarly, the azimuth matched filter is also presented by a four-order polynomial in the frequency domain, which is given by

$$H_{\text{azi}}(r_0, f_\eta) = \exp \left\{ -j \frac{4\pi}{\lambda} \left[ \frac{\lambda^2 (f_\eta - f_{\text{dc}})^2}{8} (\alpha_0 - \alpha_{\text{ref}}) - \frac{\lambda^3 (f_\eta - f_{\text{dc}})^3}{24} (\beta_0 - \beta_{\text{ref}}) + \frac{\lambda^4 (f_\eta - f_{\text{dc}})^4}{64} (\gamma_0 - \gamma_{\text{ref}}) \right] \right\}. \quad (20)$$

After multiplying (20) with the signal, the target is focused and located by applying azimuth IFT.

3) *Range Segmenting*: The aforementioned method can work well for high-resolution LEO SAR. Nevertheless, the focus depth is not sufficient for spaceborne SAR due to the residual cross-coupling phase between range and azimuth at the slant range  $r_0$  that can be described as

$$\begin{aligned} \Phi_{\text{res}}(r_0, f_r, f_\eta) &= [\Phi_{\text{PTRS}}(r_0, f_r, f_\eta) - \Phi_{\text{PTRS}}(r_{\text{ref}}, f_r, f_\eta)] \\ &\quad - [\Phi_{\text{RCM}}(r_0, f_r, f_\eta) - \Phi_{\text{RCM}}(r_{\text{ref}}, f_r, f_\eta)] \\ &\quad - [\Phi_{\text{azi}}(r_0, f_r, f_\eta) - \Phi_{\text{azi}}(r_{\text{ref}}, f_r, f_\eta)]. \end{aligned} \quad (21)$$

From (21), it is seen that the residual coupling phase increases with slant range displacement (defined as  $r_0 - r_{\text{ref}}$ ). A simulation experiment with parameters described in Section IV is followed to evaluate the focus depth in the presented situation. Fig. 7 shows the maximal residual coupling phase with respect to slant range displacements, where less than 2000-m focus depth can be obtained for the whole imaging scene. Furthermore, the focus depth is narrowed when the azimuth extent extends in the sliding spotlight mode due to the increasing Doppler centroid. Therefore, the residual cross-coupling phase should be properly handled.



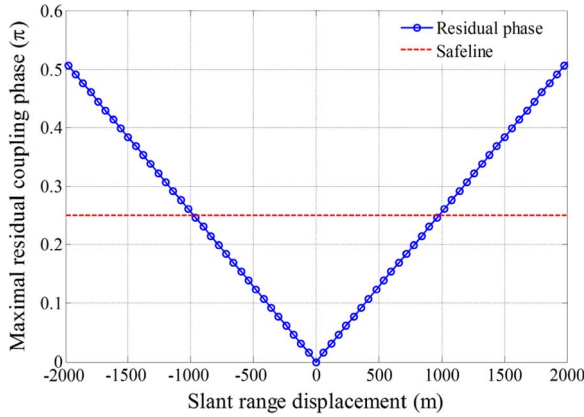


Fig. 7. High-order coupling phase as a function of slant range displacement.

It should be noted that the residual coupling phase in (21) is also spatial variant in DRM4 such that the conventional nonlinear chirp scaling operation cannot be directly applied. In the presented algorithm, we compensate the phase by range segmenting. The steps are given as follows.

- Step 1) Divide the signal into segments in the range direction with maximal residual coupling phase less than  $\pi/4$ .
- Step 2) Apply range FT to transform the segment signal into wavenumber domain.
- Step 3) Compute the compensation function  $H_{\text{comp}}(r_m, f_r, f_\eta)$  according to (21) for each segment, where the reference slant range  $r_m$  is updated to the middle slant range of each segment, and then, multiply it with the signal.
- Step 4) Apply range IFT to the segment signal.

After all segments were processed, we apply azimuth compression to the whole signal to complete the data-focusing procedure. Notice that the residual coupling phase term (21) is employed, instead of the second-order and third-order coupling phases in (14) and (15), to compensate the residual coupling phase in the algorithm. This selection ensures high performance of the proposed algorithm in high-resolution case, and we illustrate it in Appendix B.

We briefly summarize the work of this section. First, the imaging geometry of the high-resolution sliding spotlight spaceborne SAR is introduced, and then, the corresponding focusing algorithm is developed, where the conventional two-step method is applied to remove azimuth aliasing and the classic RDA is improved to focus the signal in DRM4. At last, compensation of the residual cross-coupling phase by segmenting in the range direction greatly broadens the focus depth. As a result, the issue of data focusing for high-resolution spaceborne SAR is solved. We verify it with simulation experiments in Section IV.

#### IV. SIMULATION EXPERIMENTS

Simulation experiments are performed to assess the proposed approach for the signal processing of the high-resolution sliding spotlight LEO SAR. The image quality and the accuracy of geolocation of the algorithm are both evaluated. In addition, a state-of-the-art RDA is employed for comparison [10]. First

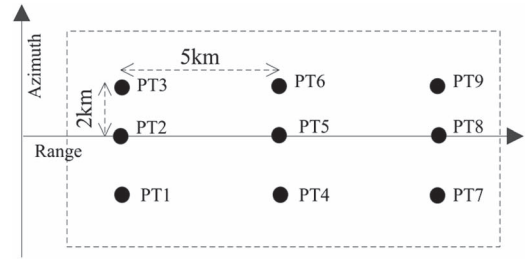


Fig. 8. Ground range scene for simulation.

TABLE I  
SIMULATION PARAMETERS

Description	value	Description	value
Perigee Altitude	668 km	Carrier frequency	9.6GHz
Eccentricity	0.0011	Bandwidth	1000MHz
Inclination	98°	Sample frequency	1133MHz
Longitude of ascend node	0°	Pulse duration	2us
Argument of perigee	90°	Slide factor	0.1
Latitude argument	45°	Antenna length	6m
Closest range	827.3km	PRF	4560Hz
Rotation range	919.2km	Velocity	7608.34m/s
Look angle	35°	Illuminated time	10.89s

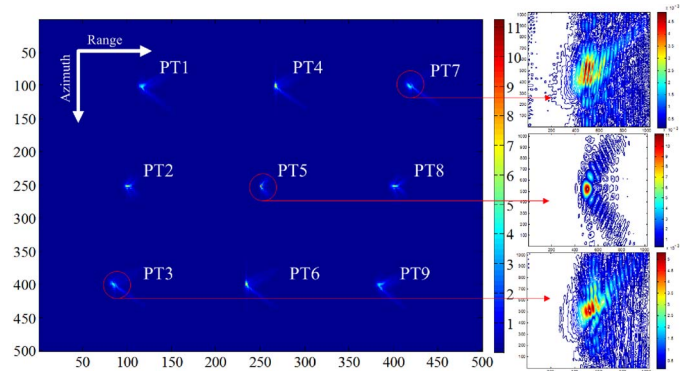


Fig. 9. Focused result by the RDA.

of all, we give the simulation scene with nine point targets uniformly distributed on ground range plane as shown in Fig. 8. A sun-synchronous orbit is designed in the simulation, and the parameters are described in Table I. The illuminated time is 10.89 s such that the azimuth resolution of 0.3 m can be achieved with azimuth extent of 4 km. The transmitted bandwidth is up to 1000 MHz to adapt the variations of look angle along range.

##### A. Image Quality Evaluation

We simulate the focused result of an updated RDA for comparison in this section, where CHRE is utilized and the corresponding velocity is calculated according to (2) for each range bin. The RCM is corrected by interpolation with updated slant range and equivalent velocity. The second range compression is also fully compensated by range segmenting. At last, the azimuth matched filtering is performed in the RDA with updated range and velocity parameters. The focused result is shown in Fig. 9. The blank districts in the focused image have been trimmed off since the simulation scene is too large to clearly distinguish the focused point targets. Fig. 9 shows that



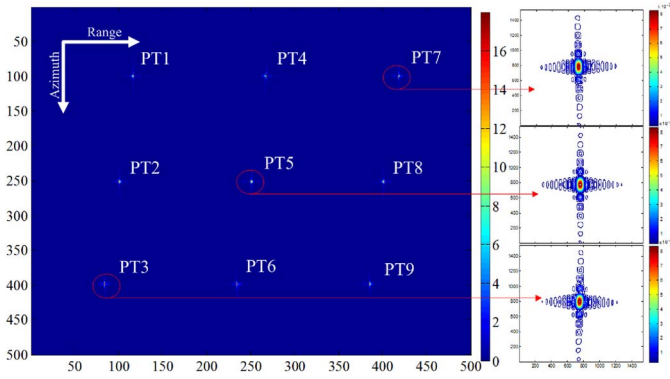


Fig. 10. Focused result using the proposed algorithm.

TABLE II  
PERFORMANCE ANALYSIS OF POINT TARGETS

	Range			Azimuth		
	IRW (m)	PSLR (dB)	ISLR (dB)	IRW (m)	PSLR (dB)	ISLR (dB)
PT1	0.132	-13.06	-9.74	0.297	-12.86	-10.49
PT2	0.132	-13.06	-9.76	0.297	-13.47	-10.84
PT3	0.132	-13.02	-9.72	0.298	-12.94	-10.63
PT4	0.133	-13.24	-10.03	0.299	-12.97	-10.57
PT5	0.132	-13.30	-10.08	0.296	-13.41	-10.88
PT6	0.133	-13.21	-10.06	0.299	-12.94	-10.61
PT7	0.133	-13.01	-9.80	0.301	-13.07	-10.68
PT8	0.132	-12.97	-9.71	0.296	-13.12	-10.62
PT9	0.132	-13.03	-9.82	0.301	-13.13	-10.74

all the point targets are severely defocused in the presented case, especially the targets at the edge of the azimuth extent.

On the contrary, with more accurate range equation and the custom-built focusing algorithm, the focusing performance is dramatically improved with the proposed algorithm so that all targets are well focused in Fig. 10. Some remarks are helpful to better understand the focused image in Fig. 10.

The different locations of PT1, PT2, and PT3 can be ascribed to the curved orbit in DRM4 due to the rotation of the Earth. The interpolated contours of PT3, PT5, and PT7 are presented to evaluate the image quality. It can be seen that all of these targets are well compressed with the proposed method. Furthermore, small squint angles can be observed in the results of PT3 and PT7 because of the beam steering in the sliding spotlight mode. To quantify the focusing performance, the point target analysis results are listed in Table II.

By comparing the analysis results of PT4, PT5, and PT6 in Table II, the peak sidelobe ratios (PSLRs) in azimuth slightly decreases along the azimuth direction. We may ascribe it to the increasing cross-coupling phase along the azimuth direction, which is beyond the proposed PTRS and is induced by the derivation of PTRS with low-order MSR.

Similarly, the PSLRs and integrated sidelobe ratios (ISLRs) in range are also slowly falling along the range direction by comparing the performances of PT2, PT5, and PT8. The interpolator for differential RCMC can mainly account for the degradation.

To better assess the image quality of the proposed method in the case of wide swath and high resolution, we make a performance statistics with all point targets in Table III, where the absolute performance variation is defined as the maximal

TABLE III  
PERFORMANCE STATISTICS

	Range		Azimuth			
	IRW	PSLR	ISLR	IRW	PSLR	ISLR
Absolute	0.0012m	0.32dB	0.37dB	0.005m	0.55dB	0.38dB
Percent	0.94%	2.45%	3.71%	1.71%	4.11%	3.57%

TABLE IV  
GEOLOCATION RESULTS OF POINT TARGETS

Point targets	Position in imaging scene (m)	Position in focused image (m)	Position deviations (m)
PT1	(827316.34, -2214.24)	(827316.44, -2214.19)	(0.10, 0.05)
PT2	(827314.17, 0.00)	(827314.19, 0.00)	(0.02, 0.00)
PT3	(827312.00, 2214.24)	(827312.07, 2214.19)	(0.07, -0.05)
PT4	(830471.53, -2214.24)	(830471.60, -2214.19)	(0.07, 0.05)
PT5	(830469.35, 0.00)	(830469.35, 0.00)	(0.00, 0.00)
PT6	(830467.17, 2214.24)	(830467.23, 2214.19)	(0.05, -0.05)
PT7	(833647.78, -2214.24)	(833647.81, -2214.19)	(0.03, 0.05)
PT8	(833645.60, 0.00)	(833645.69, 0.00)	(0.09, 0.00)
PT9	(833643.42, 2214.24)	(833643.44, 2214.19)	(0.02, -0.05)

variation referred to the value of PT5 and the percent one is the ratio of the absolute variation and the value of PT5.

Table III demonstrates a high focusing performance for the whole scene. The deterioration of the impulse response widths (IRWs) in the range direction is less than 1% and that in azimuth direction is also better than 2%. The PSLRs and ISLRs demonstrate less than 5% degradation in the azimuth direction, while the performance is better in the range direction. Therefore, considering the wide swath of the imaging scene and the little deterioration of the focusing performance, we can draw the conclusion that the proposed DRM4 and the corresponding focusing algorithm can handle the image formation of the high-resolution sliding spotlight LEO SAR.

### B. Geolocation Analysis

For the evaluation of a new imaging processor, geolocation of point targets in the compressed image has the equal weight as the focusing quality. Table IV shows the position deviations of all targets after compressed, where the slant range imaging plane is taken as reference plane.

In Table IV, the position of PT5 is taken as reference since its slant range is used for reference slant range in our algorithm, leading to zero position deviations. Nevertheless, we can observe that other targets show position deviations both in the range and azimuth directions. The deviation in range is less than a range bin (0.132 m) and that in azimuth is only 0.05 m, showing high geolocation accuracy of the algorithm. Consequently, we can conclude that the proposed SAR imaging processor enjoys outstanding performance on focusing quality as well as geolocation for the signal processing of high-resolution spaceborne SAR.

## V. CONCLUSION

This paper has presented a novel high-order range equation model for high-resolution LEO SAR, and the corresponding imaging approach has been put forward. Fourth-order Doppler parameters are involved in the proposed range equation so that it is prevailing to its predecessors. As a result, a higher azimuth

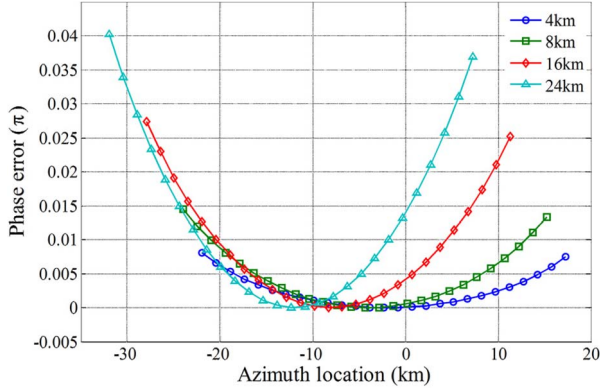


Fig. 11. Phase error due to the approximation of Doppler parameters in azimuth direction with different azimuth extents.

resolution can be accommodated by this model. Furthermore, the signal model of DRM4 has been presented, as well as PTRS. Based on the signal model, an extended range Doppler domain focusing algorithm has been developed to handle the signal processing, and the simulation experiments validate its accuracy and advantages. However, only a general case is given in this paper. There are still a lot of issues that should be studied for high-resolution spaceborne SAR, such as a more efficient imaging algorithm with acceptable approximation and the system parameter design as well as a more accurate PTRS with higher order MSR. We will focus on the remaining issues in the future work.

#### APPENDIX A

##### APPROXIMATION OF DOPPLER PARAMETERS IN THE AZIMUTH DIRECTION

In the design of the imaging algorithm for high-resolution LEO SAR, we assume that all targets with the same nearest range in the imaging scene share the same Doppler parameters of DRM4 as described in Section III, i.e., we suppose that PT1 and PT2 in Fig. 5 (assume that they have the same nearest ranges) share the same parameters of range equation. It is essential for the proposed algorithm to work well without segmenting in azimuth. However, the assumption would introduce extra phase error in the azimuth matched filter, especially in the case of high resolution. Consequently, it is a must to discuss it to determine the maximal azimuth extent of the focusing algorithm.

First of all, we give the range equations of PT1 and PT2 in (A1) and (A2), respectively

$$R_{PT1}(\eta') = r_{01} + k'_1\eta' + k'_2\eta'^2 + k'_3\eta'^3 + k'_4\eta'^4 \quad (A1)$$

$$R_{PT2}(\eta) = r_{02} + k_1\eta + k_2\eta^2 + k_3\eta^3 + k_4\eta^4 \quad (A2)$$

where  $r_{01}$ ,  $r_{02}$  represent the nearest range of PT1 and PT2, while the corresponding azimuth times are  $\eta'$ ,  $\eta$ , respectively.  $k'_1, \dots, k'_4$  are the Doppler parameters of PT1, and  $k_1, \dots, k_4$  denote those of PT2.

In the focusing approach,  $k'_1 \approx k_1, \dots, k'_4 \approx k_4$ , and thus, the slant range error is induced as (A3) expresses, where  $\Delta r_{DRM4}$  is the intrinsic slant range error of DRM4 for PT1

$$\Delta R_1 = (k'_1 - k_1)\eta' + (k'_2 - k_2)\eta'^2 + (k'_3 - k_3)\eta'^3 + (k'_4 - k_4)\eta'^4 + \Delta r_{DRM4}. \quad (A3)$$

The phase error introduced by the slant range error is defined as  $4\pi\Delta R_1/\lambda$ , and  $\lambda$  is a wavelength with a value of 0.03125 m. We simulate the phase error with PT1 located at 2, 4, 8, and 12 km in the azimuth direction in strip-map mode. The simulation parameters are described in Section IV, and the results as a function of the azimuth extent are plotted in Fig. 11.

The results in Fig. 11 reveal that the phase errors due to the assumption are all very small, with different azimuth extents so that it can be ignored in the data processing of LEO SAR. Consequently, the assumption is validated.

#### APPENDIX B

##### COUPLING PHASE IN DRM4

In this section, the cross-coupling terms in DRM4 are discussed. To highlight the effect of these terms in the proposed focusing algorithm, both broadside and low-squint configurations are simulated, where the IRW, PSLR, and ISLR are used as criteria to quantify the effect.

The second-order, third-order, and high-order coupling phases are denoted as  $\Phi_{\text{couple2}}(r_0, f_r, f_\eta)$ ,  $\Phi_{\text{couple3}}(r_0, f_r, f_\eta)$ , and  $\Phi_{\text{couple}}(r_0, f_r, f_\eta)$ , respectively, which can be expressed as (B1)–(B3) from Section II. Two simulation experiments are carried out to evaluate the effect of these coupling phases in the data focusing of high-resolution spaceborne SAR

$$\begin{aligned} \Phi_{\text{couple2}}(r_0, f_r, f_\eta) \\ = \Phi_{\text{az\_rg2}}(r_0, f_r, f_\eta) + \pi f_r^2 / K_r \end{aligned} \quad (B1)$$

$$\begin{aligned} \Phi_{\text{couple3}}(r_0, f_r, f_\eta) \\ = \Phi_{\text{couple2}}(r_0, f_r, f_\eta) + \Phi_{\text{az\_rg3}}(r_0, f_r, f_\eta) \end{aligned} \quad (B2)$$

$$\begin{aligned} \Phi_{\text{couple}}(r_0, f_r, f_\eta) \\ = \Phi_{\text{PTRS}}(r_0, f_r, f_\eta) + \Phi_{\text{RCM}}(r_0, f_r, f_\eta) \\ - \Phi_{\text{azi}}(r_0, f_r, f_\eta) + \pi f_r^2 / K_r. \end{aligned} \quad (B3)$$

##### A. Broadside Configuration

The broadside configurations are described in Section IV, where the transmitted bandwidth is 1000 MHz and the PRF after azimuth preprocessing is 31 098 Hz. A point target (PT2) that is located at the center of the simulation scene is considered. We perform data focusing with the aforementioned coupling phases compensated, and the results are shown in Fig. 12.

It can be observed from Fig. 12(a) that the image quality severely deteriorates with only the second-order coupling phase compensated. The residual coupling phase that is defined as the coupling phase described by subtracting (B3) to that of (B1) is depicted in Fig. 13(a), and it is much greater than  $\pi/4$ , which must be compensated in the proposed focusing algorithm.

By comparing Fig. 12(b) and (c), we can draw the following conclusion. First, with the high-order coupling phase fully compensated, the point target can be compressed well, and it proves that our proposed PTRS can deal with the high-resolution spaceborne SAR signal processing in broadside configuration. Second, there is little focusing performance degradation when the third-order coupling phase is compensated, which reveals that third-order or higher order coupling terms should be taken

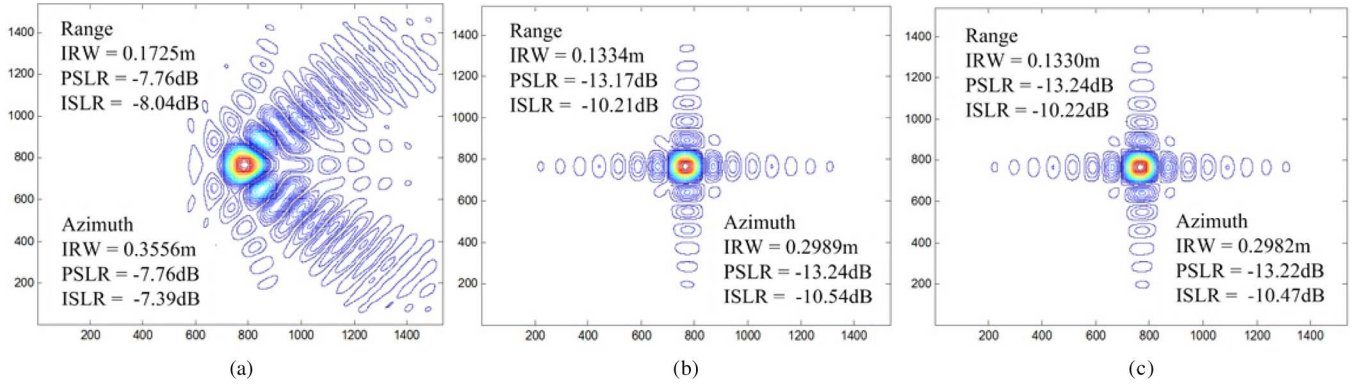


Fig. 12. (a) Focused result with second-order coupling phase compensated. (b) Focused result with third-order coupling phase compensated. (c) Focused result with high-order coupling phase compensated.

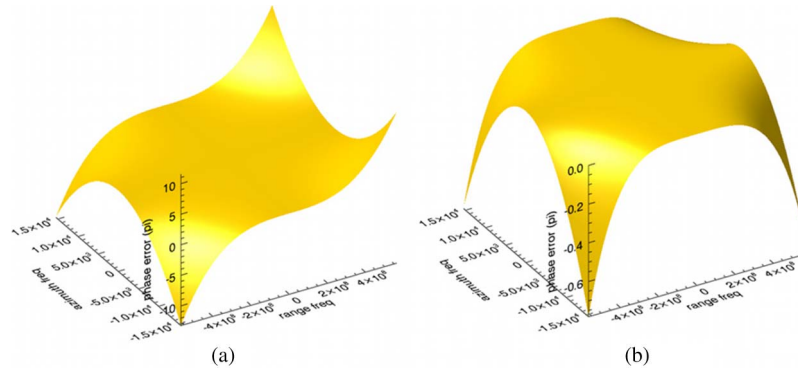


Fig. 13. (a) Residual coupling phase for the second-order coupling term. (b) Residual coupling phase for the third-order coupling term.

TABLE V  
CONFIGURATIONS FOR LOW-SQUINT MODE

Configuration No	Config.1	Config.2	Config.3
Transmitted bandwidth	500MHz	1000MHz	1000MHz
Doppler centroid	13187Hz	13187Hz	18456Hz
maximal squint angle	1.6°	1.6°	2.17°
Equivalent azimuth extent	5000m	5000m	7000m

into consideration even in broadside configuration. To quantify the degradation, we depict the residual coupling phase for the third-order coupling term in Fig. 13(b), which is defined in the same way as Fig. 13(a), and it is still great so that it cannot be neglected in the focusing algorithm.

Therefore, in this section, the cross-coupling terms of the signal with DRM4 in broadside configuration is discussed, and results show that the third-order and higher order coupling phases should be taken into account in the focusing algorithm of high-resolution spaceborne SAR.

### B. Low-Squint Configuration

The steering of the antenna during the data acquisition of the sliding spotlight SAR leads to a low-squint beam for the targets at the edge of the azimuth scene. Hence, it is a must to evaluate the capability of the derived PTRS model in low-squint mode. Three low-squint configurations are listed in Table V, and the high-order cross-coupling term in (B3) is considered in the following simulations.

In the simulation, the point target (PT3) is located at the edge of the azimuth scene. Different squint angles and transmitted

bandwidths are configured to evaluate the performance of the proposed PTRS model with large bandwidth and large azimuth scene extent in sliding spotlight mode. Fig. 14 shows the results.

There is little focusing quality degradation with bandwidth increases, which is in contrast with that of Fig. 14(a) and (b), proving that the derived PTRS model can accommodate the low-squint-angle case with large transmitted bandwidth. However, with higher squint angle configured in configuration 3, we can observe that the PSLR of the focused result in Fig. 14(c) deteriorates about 0.6 dB compared with that of the low-squint case. It seems that the higher order coupling phase approximation in the derivation of the PTRS by low-order MSR can account for the degradation since it is dependent on the transmitted bandwidth and the azimuth frequency.

Therefore, with the simulation of three configurations, we can draw the following conclusion. On the one hand, the proposed PTRS model is well suited for the low squint angle with large transmitted bandwidth in sliding spotlight spaceborne SAR. On the other hand, a more accurate method or a higher order MSR should be advised for the derivation of PTRS in the case of high squint and high resolution so that the higher order coupling phase beyond the presented PTRS can be accommodated.

### ACKNOWLEDGMENT

The authors would like to thank the Spaceborne Microwave Remote Sensing System Department, Institute of Electronics,



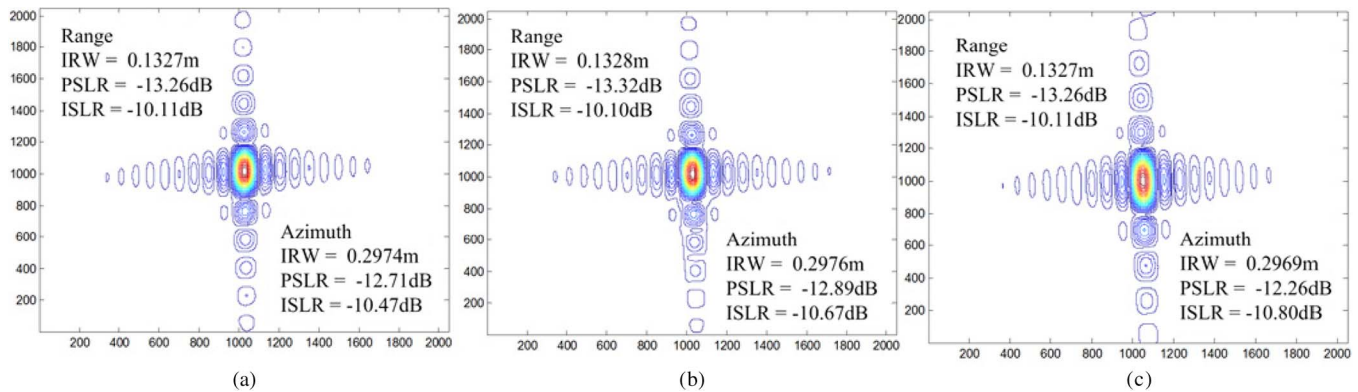


Fig. 14. (a) Focused result with configuration 1. (b) Focused result with configuration 2. (c) Focused result with configuration 3.

Chinese Academy of Sciences, Beijing, China, for providing great support and B. Cheung of the University of California, Davis, CA, USA, for improving this paper.

## REFERENCES

- [1] W. Townsend, "An initial assessment of the performance achieved by the Seasat-1 radar altimeter," *IEEE J. Ocean. Eng.*, vol. OE-5, no. 2, pp. 80–92, Apr. 1980.
- [2] F. Caltagirone, P. Spera, and R. Vigliotti, "SkyMed/COSMO mission overview," in *Proc. IGARSS*, Seattle, WA, USA, 1998, pp. 683–685.
- [3] U. Naftaly and R. Levy-Nathansohn, "Overview of the TecSAR satellite hardware and mosaic mode," *IEEE Geosci. Remote Sens. Lett.*, vol. 5, no. 3, pp. 423–426, Jul. 2008.
- [4] L. Brule, D. Delisle, H. Baeggli, and J. Graham, "RADARSAT-2 program update," in *Proc. IGARSS*, 2005, pp. 9–11.
- [5] Z. Lu, R. Fatland, M. Wyss, S. Li, J. Eichelberger, K. Dean, and J. Freymueller, "Deformation of new trident volcano measured by ERS-I SAR interferometry, Katmai National Park, Alaska," *Geophys. Res. Lett.*, vol. 24, no. 6, pp. 695–698, Mar. 1997.
- [6] M. Migliaccio, A. Gambardella, F. Nunziata, M. Shimada, and O. Isoguchi, "ALOS-PALSAR polarimetric SAR data to observe sea oil slicks," in *Proc. IGARSS*, Cape Town, South Africa, 2009, pp. IV-669–IV-672.
- [7] H. Breit, T. Fritz, U. Balss, M. Lachaise, A. Niedermeier, and M. Vonavka, "TerraSAR-X SAR processing and products," *IEEE Trans. Geosci. Remote Sens.*, vol. 48, no. 2, pp. 727–740, Feb. 2010.
- [8] L. J. Huang, X. L. Qiu, D. H. Hu, and C. B. Ding, "Focusing of medium-earth-orbit SAR with advanced nonlinear chirp scaling algorithm," *IEEE Trans. Geosci. Remote Sens.*, vol. 49, no. 1, pp. 500–508, Jan. 2011.
- [9] K. Tomiyasu, "Synthetic aperture radar imaging from an inclined geosynchronous orbit," *IEEE Trans. Geosci. Remote Sens.*, vol. GE-21, no. 3, pp. 324–329, Jul. 1983.
- [10] I. G. Cumming and F. H. Wong, *Digital Processing of Synthetic Aperture Radar Data: Algorithms and Implementation*. Norwood, MA, USA: Artech House, 2005.
- [11] A. Moreira and Y. Huang, "Airborne SAR processing of highly squinted data using a chirp scaling approach with integrated motion compensation," *IEEE Trans. Geosci. Remote Sens.*, vol. 32, no. 5, pp. 1029–1040, Sep. 1994.
- [12] A. Moreira, J. Mittermayer, and R. Scheiber, "Extended chirp scaling algorithm for air- and spaceborne SAR data processing in stripmap and ScanSAR imaging modes," *IEEE Trans. Geosci. Remote Sens.*, vol. 34, no. 5, pp. 1123–1136, Sep. 1996.
- [13] K. Eldhuset, "A new fourth-order processing algorithm for spaceborne SAR," *IEEE Trans. Aerosp. Electron. Syst.*, vol. 34, no. 3, pp. 824–835, Jul. 1998.
- [14] C. W. Chen, "Modified polar format algorithm for processing spaceborne SAR data," in *Proc. IEEE Int. Radar Conf.*, Apr. 2004, pp. 44–49.
- [15] A. Boag, Y. Bresler, and E. Michielssen, "A multilevel domain decomposition algorithm for fast  $O(N^2 \log(N))$  reprojection of tomographic images," *IEEE Trans. Image Process.*, vol. 9, no. 9, pp. 1573–1582, Sep. 2000.
- [16] Y. Ding and D. C. Munson, Jr., "A fast back-projection algorithm for bistatic SAR imaging," in *Proc. IEEE Int. Conf. Image Process.*, 2002, vol. 2, pp. II-449–II-452.
- [17] L. M. H. Ulander, H. Hellsten, and G. Stenström, "Synthetic-aperture radar processing using fast factorized back-projection," *IEEE Trans. Aerosp. Electron. Syst.*, vol. 39, no. 3, pp. 760–776, Jul. 2003.
- [18] K. Li, D. N. Held, J. Curlander, and C. Wu, "Doppler parameter estimation for spaceborne synthetic aperture radars," *IEEE Trans. Geosci. Remote Sens.*, vol. GE-23, no. 1, pp. 47–56, Jan. 1985.
- [19] C. Y. Chang and J. C. Curlander, "Doppler centroid ambiguity estimation for synthetic aperture radars," in *Proc. IGARSS*, Vancouver, BC, Canada, 1989, pp. 2567–2571.
- [20] W. G. Carrara, R. S. Goodman, and R. M. Majewski, *Spotlight Synthetic Aperture Radar: Signal Processing Algorithms*. Norwood, MA, USA: Artech House, 1995.
- [21] *Lacrosse Introduction*. [Online]. Available: <http://en.wikipedia.org/wiki/Lacrosse>
- [22] B. J. Zhao, X. Y. Qi, Y. K. Deng, R. Wang, and H. J. Song, "Accurate fourth-order Doppler parameter estimation approach for geosynchronous SAR," in *Proc. EUSAR*, Nurnberg, Germany, Apr. 2012, pp. 615–618.
- [23] Fiedler, E. Boerner, J. Mittermayer, and G. Krieger, "Total zero Doppler steering—A new method for minimizing the Doppler centroid," *IEEE Geosci. Remote Sens. Lett.*, vol. 2, no. 2, pp. 141–145, Apr. 2005.
- [24] J. C. Curlander and R. N. McDonough, *Synthetic Aperture Radar: Systems and Signal Processing*. New York, NY, USA: Wiley, 1991.
- [25] Y. L. Neo, F. H. Wong, and I. G. Cumming, "A two-dimensional spectrum for bistatic SAR processing using series reversion," *IEEE Geosci. Remote Sens. Lett.*, vol. 4, no. 1, pp. 93–96, Jan. 2007.
- [26] Y. L. Neo, F. H. Wong, and I. G. Cumming, "Processing of azimuth-invariant bistatic SAR data using the range Doppler algorithm," *IEEE Trans. Geosci. Remote Sens.*, vol. 46, no. 1, pp. 14–21, Jan. 2008.
- [27] R. Lanari, M. Tesauro, E. Sansosti, and G. Fornaro, "Spotlight SAR data focusing based on a two-step processing approach," *IEEE Trans. Geosci. Remote Sens.*, vol. 39, no. 9, pp. 1993–2004, Sep. 2001.
- [28] J. Mittermayer, A. Moreira, and O. Loffeld, "Spotlight SAR data processing using the frequency scaling algorithm," *IEEE Trans. Geosci. Remote Sens.*, vol. 37, no. 5, pp. 2198–2214, Sep. 1999.
- [29] F. F. Liu, Z. G. Ding, T. Zeng, and T. Long, "Performance analysis of two-step algorithm in sliding spotlights space-borne SAR," in *Radar Conference*, Washington, DC, USA, May 2010, pp. 965–968.
- [30] Y. Liu, M. Xing, G. Sun, X. Lv, Z. Bao, W. Hong, and Y. Wu, "Echo model analyses and imaging algorithm for high-resolution SAR on high-speed platform," *IEEE Trans. Geosci. Remote Sens.*, vol. 50, no. 3, pp. 933–950, Mar. 2012.



compensation.

**Yunhua Luo** received the B.S. degree from Central South University, Changsha, China, in 2009. In September 2009, he enrolled in the Institute of Electronics, Chinese Academy of Sciences (IECAS), Beijing, China. He is currently working toward the Ph.D. degree in the Department of Space Microwave Remote Sensing System, IECAS.

His current research interests include high-resolution spaceborne synthetic aperture radar (SAR) signal processing, frequency-modulated continuous wave SAR signal processing, and motion





**Bingji Zhao** received the B.S. degree in electronic engineering and information science from the Ha'er Bin Engineering University, Heilongjiang, China, in 2007 and the Ph.D. degree in communication and information systems from the Institute of Electronics, Chinese Academy of Sciences, Beijing, China, in 2013.

His current research interests are geosynchronous synthetic aperture radar (GEO SAR) and low earth orbital high-resolution spaceborne SAR system design and signal processing.



**Xiaolei Han** received the B.S. degree in electronic engineering from the Xi'an Institute of Electronic and Telecommunication, Xi'an, China, in 2006 and the Ph.D. degree from the Institute of Electronics, Chinese Academy of Sciences, Beijing, China, in 2013.

His main interests are synthetic aperture radar system design and signal processing.



**Robert Wang** (M'07–SM'12) received the B.S. degree in control engineering from the University of Henan, Kaifeng, China, in 2002 and the Dr.Eng. degree from the Graduate University, Chinese Academy of Sciences, Beijing, China, in 2007.

In 2007, he joined the Center for Sensorsystems (ZESS), University of Siegen, Siegen, Germany. He was appointed as a Research Fellow with the Institute of Electronics, Chinese Academy of Sciences (IECAS), Beijing, where he was selected as a member of the Academic Committee in 2012. He has been involved in the following projects: TerraSAR-X/PAMIR hybrid bistatic synthetic aperture radar (SAR) experiment, PAMIR/stationary bistatic SAR experiment, PAMIR/stationary bistatic SAR experiment with nonsynchronized oscillators, 3-D/4-D SAR tomography for high-resolution information extraction and monitoring Earth's dynamics, millimeter-wave frequency-modulated continuous wave (FMCW) SAR data processing, and so on. In addition, he has been involved in some SAR projects for Fraunhofer-FHR. He has proposed several bistatic SAR spectral models to formulate the complex bistatic SAR configurations, obtaining the TerraSAR-X/PAMIR hybrid bistatic SAR image in the frequency domain for the first time. He proposed an analytical continuous-wave SAR spectrum model which can reveal the essential characteristic of the in-pulse motion. He is currently responsible for several National High-Resolution Earth Observation Major Special projects. Since 2012, he has been the Coprincipal Investigator for Helmholtz-CAS Joint Research Group concerning spaceborne microwave remote sensing for prevention and forensic analysis of natural hazards and extreme events. He has published more than 120 papers since 2003, of which more than 40 are peer-reviewed and well-known journal papers, including more than 10 papers published in IEEE TRANSACTIONS ON GEOSCIENCE AND REMOTE SENSING. He is the author of a tutorial entitled "Results and progresses of advanced bistatic SAR experiments" presented at the European Radar Conference 2009 and the coauthor of a tutorial entitled "Progress in bistatic SAR concepts and algorithms" presented at the European Conference on Synthetic Aperture Radar (EUSAR) 2008. His current research interests include monostatic and bistatic SAR imaging, multibaseline for monostatic and bistatic SAR interferometry, and high-resolution spaceborne SAR systems and FMCW SAR systems.

Dr. Wang was chosen in the "Hundred Talents Program" of the Chinese Academy of Sciences in 2011 and subsequently succeeded in the review "Overseas Outstanding Talent." In 2012, he became a Senior Member of the IEEE Geoscience and Remote Sensing Society. He has contributed to invited sessions on bistatic SAR at EUSAR 2008 and 2010. He was chosen as the Session Chair of EUSAR 2012 and IGARSS 2012.



**Hongjun Song** received the B.E. degree in electronics from the University of Science and Technology of China, Hefei, China, in 1991 and the M.E. and Ph.D. degrees from the Institute of Electronics, Chinese Academy of Sciences (IECAS), Beijing, China, in 1994 and 1998, respectively.

Since 1994, he has been with IECAS, where he worked on the system design and simulation of spaceborne synthetic aperture radar (SAR) system/signal processing. His current interests include signal processing and system design of novel SAR

modes.



**Yunkai Deng** (M'11) received the M.S. degree in electrical engineering from the Beijing Institute of Technology, Beijing, China, in 1993.

In 1993, he joined the Institute of Electronics, Chinese Academy of Sciences (IECAS), Beijing, where he worked on antenna design, microwave circuit design, and spaceborne/airborne synthetic aperture radar (SAR) technology. He has been the leader of several spaceborne/airborne SAR programs and has developed some key technologies of spaceborne/airborne SAR. He is currently a Research

Scientist, a member of the Scientific Board, and the Director of the Spaceborne Microwave Remote Sensing System Department, IECAS. Since 2012, he has been a Principal Investigator for Helmholtz-CAS Joint Research Group concerning spaceborne microwave remote sensing for prevention and forensic analysis of natural hazards and extreme events. He has published more than 100 papers since 2002, of which more than 40 are peer-reviewed and well-known journal papers. His current research interests include spaceborne/airborne SAR technology for advanced modes, multifunctional radar imaging, and microwave circuit design.